Journal of Physics: Condensed Matter

PAPER

Determination of the tricritical point, *H*–*T* phase diagram and exchange interactions in the antiferromagnet $MnTa_2O_6$

To cite this article: Maruthi R *et al* 2022 *J. Phys.: Condens. Matter* **34** 155801

IOP Publishing Journal of Physics: Condensed Matter
J. Phys.: Condens. Matter **34** (2022) 155801 (11pp) https://doi.org/10.1088/1361-648X/ac4cec

Determination of the tricritical point, *H–T* phase diagram and exchange interactions in the antiferromagnet $MnTa_2O_6$

Maruthi R[1], Mohindar S Seehra[2], Sayandeep Ghosh[1], Rohit Medwal[3], Rajdeep S Rawat[3], Bruno Weise[4], Eun Sang Choi[5] and Subhash Thota[1,*]

[1] Department of Physics, Indian Institute of Technology Guwahati, 781039, Assam, India
[2] Department of Physics and Astronomy, West Virginia University, Morgantown, WV 26506, United States of America
[3] National Institute of Education, Nanyang Technological University, Singapore 637616, Singapore
[4] Leibniz-IFW Dresden, Institute for Complex Materials, D-01069 Dresden, Germany
[5] National High Magnetic Field Laboratory, Tallahassee, FL 32310-3706, United States of America

E-mail: subhasht@iitg.ac.in

Received 7 November 2021, revised 6 January 2022
Accepted for publication 19 January 2022
Published 7 February 2022

Abstract

Using the analysis of the temperature and magnetic field dependence of the magnetization (M) measured in the temperature range of 1.5 K to 400 K in magnetic fields up to 250 kOe, the magnetic field-temperature (H–T) phase diagram, tricritical point and exchange constants of the antiferromagnetic $MnTa_2O_6$ are determined in this work. X-ray diffraction/Rietveld refinement and x-ray photoelectron spectroscopy of the polycrystalline $MnTa_2O_6$ sample verified its phase purity. Temperature dependence of the magnetic susceptibility χ $(= M/H)$ yields the Néel temperature $T_N = 5.97$ K determined from the peak in the computed $\partial(\chi T)/\partial T$ vs T plot, in agreement with the $T_N = 6.00$ K determined from the peak in the C_P vs T data. The experimental data of C_P vs T near T_N is fitted to $C_P = A|T - T_N|^{-\alpha}$ yielding the critical exponent $\alpha = 0.10(0.13)$ for $T > T_N$ ($T < T_N$). The χ vs T data for $T > 25$ K fits well with the modified Curie–Weiss law: $\chi = \chi_0 + C/(T - \theta)$ with $\chi_0 = -2.12 \times 10^{-4}$ emu mol^{-1} Oe^{-1} yielding $\theta = -24$ K, and $C = 4.44$ emu K mol^{-1} Oe^{-1}, the later giving magnetic moment $\mu = 5.96\ \mu_B$ per Mn^{2+} ion. This yields the effective spin $S = 5/2$ and $g = 2.015$ for Mn^{2+}, in agreement with $g = 2.0155$ measured using electron spin resonance spectroscopy. Using the magnitudes of θ and T_N and molecular field theory, the antiferromagnetic exchange constants $J_0/k_B = -1.5 \pm 0.2$ K and $J_\perp/k_B = -0.85 \pm 0.05$ K for Mn^{2+} ions along the chain c-axis and perpendicular to the c-axis respectively are determined. The χ vs T data when compared to the prediction of a Heisenberg linear chain model provides semiquantitative agreement with the observed variation. The H–T phase diagram is mapped using the M–H isotherms and M–T data at different H yielding the tricritical point T_{TP} $(H, T) = (17.0$ kOe, 5.69 K) separating the paramagnetic, antiferromagnetic, and spin-flop phases. At 1.5 K, the experimental magnitudes of the exchange field $H_E = 206.4$ kOe and spin-flop field $H_{SF} = 23.5$ kOe yield the anisotropy field $H_A = 1.34$ kOe. These results for $MnTa_2O_6$ are compared with those reported recently in the isostructural $MnNb_2O_6$.

* Author to whom any correspondence should be addressed.

Keywords: tricritical point, H–T phase diagram, exchange interactions, antiferromagnet

(Some figures may appear in colour only in the online journal)

1. Introduction

The transition metal compounds with general chemical formula AB_2O_6 (A = Mn, Fe, Co, Ni and B = Nb, Ta) crystallize in the orthorhombic crystal structure of columbite ($FeNb_2O_6$) with four molecular formula per unit cell [1–5] except $FeTa_2O_6$,$CoTa_2O_6$ and $NiTa_2O_6$ which crystallize into tetragonal (tri-rutile) crystal structure with two molecular formula per unit cell [6–9]. In AB_2O_6 compounds usually A and B sites are occupied by divalent and pentavalent cations respectively, forming octahedra [AO_6 andBO_6] with six oxygen atoms [3, 5]. These compounds have potential applications in the field of satellite and mobile communications as dielectric resonators and filters [6, 10–12], as electrochemical gas sensors [6, 13], and in supercapacitors [6, 12].

Like $MnNb_2O_6$,$MnTa_2O_6$ also crystallizes in the columbite orthorhombic crystal structure with four formula units per cell (space group $Pbcn - D_{2h}^{14}$, N 60, oP36) but it has slightly larger unit cell parameters of $a = 14.4478$ Å, $b = 5.7677$ Å, and $c = 5.0943$ Å [6, 14] compared to $a = 14.4204$ Å, $b = 5.7566$ Å, and $c = 5.0784$ Å for $MnNb_2O_6$ [15–18]. Whereas the magnetic properties of $MnNb_2O_6$ have been reported by several previous investigators [15–18] including our own recent work in which we reported complete details of its magnetic field-temperature (H–T) phase diagram below its Neel temperature $T_N = 4.36$ K and determination of the exchange constants [18], the magnetic properties of $MnTa_2O_6$ are relatively unexplored. Although Gulyaeva *et al* [6] recently reported on the high temperature (300 K to 1203 K) heat capacity and thermal expansion measurements of $MnTa_2O_6$, the only known magnetic studies are those by Weitzel and Klein [14] in $MnTa_2O_6$ and Schraf and Weitzel in $Mn(Nb_{0.5}Ta_{0.5})_2O_6$ [19], both using neutron diffraction only. These studies reported $T_N = 5.7$ K and 5.2 K for $MnTa_2O_6$ and $Mn(Nb_{0.5}Ta_{0.5})_2O_6$ respectively compared to $T_N = 4.4$ K for $MnNb_2O_6$ thus showing that T_N increases when Ta replaces Nb in this structure.

Because of the dearth of magnetic studies in $MnTa_2O_6$ using the temperature and magnetic field dependence of magnetization, we undertook such studies in a polycrystalline sample of $MnTa_2O_6$ and our results are reported here. The polycrystalline sample of $MnTa_2O_6$ synthesized using the solid-state reaction method was structurally characterized with x-ray diffraction combined with Rietveld refinement and oxidation states of Mn^{2+},Ta^{5+} and O^{2-} ions were determined by x-ray photoelectron spectroscopy (XPS) measurements. Heat capacity measurements were used to determine the characteristics of the singularity near the Neel temperature $T_N = 5.98 \pm 0.02$ K and electron spin resonance yielded the g-value of 2.0155 characteristic of Mn^{2+} ions with $S = 5/2$ ground state. Analysis of the detailed data of the temperature and magnetic field dependence of magnetization (M) covering the temperature range of 1.5 K to 400 K in magnetic fields up to 250 kOe is used to map out the H–T phase diagram involving the spin-flop field and the magnetic tricritical or triple point T_{TP} (H, T) and this phase diagram is compared with that of $MnNb_2O_6$ reported recently [18]. Finally, the temperature dependence of the paramagnetic susceptibility for $T > T_N$ is used to determine the exchange constants of the system. These results, their discussion, and analysis are presented below.

2. Synthesis and structural characterization

Bulk sample of polycrystalline $MnTa_2O_6$ was prepared using a standard solid-state reaction method starting with stoichiometric proportions of MnO_2 and Ta_2O_5 and grounding the mixture in an agate mortar with pestle for about 6 h. The grounded homogeneous mixture was pressed into cylindrical pellets of 12 mm diameter and thickness of one mm with the help of hydraulic press. The pressed pellets were fired at 1200°C for 24 h as first sintering in air. Again, the first sintered pellets were re-grounded, pelletized, and re-sintered at 1250°C for 36 h.

The phase purity and crystal structure of this bulk samples were investigated using the Rigaku x-ray diffractometer (model: TTRAX III) with CuKα ($\lambda = 1.5406$ Å) radiation. The x-ray diffraction pattern was recorded from $2\theta = 10°$ to 80° with step size = 0.02° and scan rate 2° per minute. The Rietveld refinement of pure phase room temperature XRD pattern is shown in figure 1. The refinement is carried out with the help of FullProf programme confirms the absence of secondary phases in the compound and yielded the refined lattice parameters $a = 14.4468(8)$ Å, $b = 5.7664(3)$ Å and $c = 5.0924(4)$ Å close to the magnitudes of $a = 14.4478$ Å, $b = 5.7677$ Å and $c = 5.0943$ Å reported in the recent paper by Gulyaeva *et al* [6]. From our analysis, the bond lengths and bond angles are found to be Mn–O $\sim$ 2.205 Å; Ta–O $\sim$ 2.038 Å and Mn–O–Mn $\sim$ 95.4°; Ta–O–Ta $\sim$ 96.5°; Mn–O–Ta $\sim$ 127.4° respectively. This structure has zig-zag chains of Mn^{2+} ions along the c-axis and forming -Mn–Ta–Ta–Mn–Ta–Ta–Mn- chains along the a-axis. In the a–b plane Mn^{2+} ions are arranged in isosceles triangular geometry with exchange interactions between them [1, 20, 23] as shown in figure 2. The exchange interactions among Mn^{2+} ions in $MnTa_2O_6$ are interpreted by using the Hamiltonian [1, 21–23],

$$H = -J_0 \sum_i S_i^z S_{i+1}^z - J_1 \sum_{<ij>} \vec{S}_i.\vec{S}_j - J_2 \sum_{<ij>} \vec{S}_i.\vec{S}_j. \quad (1)$$

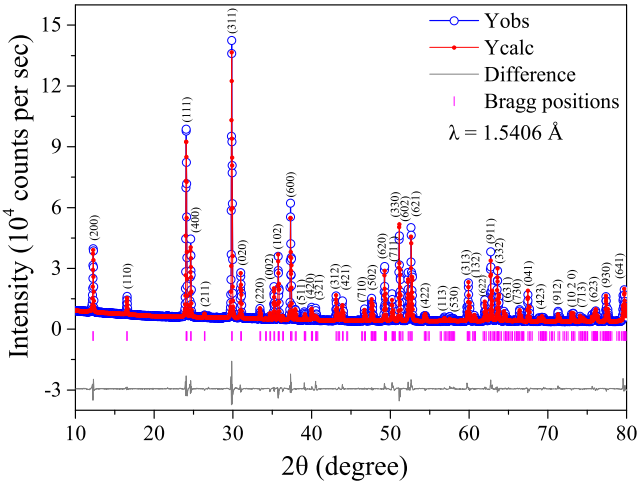

Figure 1. X-ray diffraction pattern (intensity vs Bragg angle (2θ)) of $MnTa_2O_6$ along with the Rietveld refined data and marked positions of Bragg lines. The grey line at the bottom signifies the difference between experimentally measured data and the pattern developed by a software.

Here J_0 and J_1 are the intrachain and interchain nearest neighbour exchange interactions along the c-axis and b-axis respectively, where J_2 is the next nearest exchange interaction in the a–b plane.

The electronic structure and chemical composition of the sample were probed using an x-ray photoelectron spectrometer (XPS) from Kratos Analytical (model: AXIS Supra+) configured with a dual monochromatic x-ray source Al Kα/Ag Lα (2984.2 eV) with spatial resolution less than 1 μm. The core-level electronic spectra of Mn, Ta and oxygen in $MnTa_2O_6$ are calibrated by considering the binding energy of carbon C-1s orbital ($\sim$285 eV) as reference shown in the figure 3. The Mn-2p core-level spectrum is deconvoluted into six peaks out of four are main peaks at 640.94 eV (M_1), 642.51 eV (M_2), 652.91 eV (M_3), and 654.4 eV (M_4), the other two are broad satellite peaks at 644.64 eV (S_1) and 656.88 eV (S_2) shown in the figure 3(a). The spin–orbit splitting between the main peaks of Mn-2$p_{1/2}$ and Mn-2$p_{3/2}$ i.e. ΔE (M_3–M_1) $\sim$ 11.97 eV and ΔE (M_4–M_2) $\sim$ 11.89 eV predicts the divalent oxidation state of Mn [24]. The electronic spectra of O-1s orbital is deconvoluted into two Gaussian–Lorentzian peaks, one with higher intensity peaked at 530.3 eV due to metal-lattice oxygen (Mn–O and Ta–O) bonding and the other at 531.69 eV as a satellite peak arises due to surface-absorbed oxygen shown in the figure 3(b) [25]. The deconvolution of Ta-4f core-level spectrum leads to two main peaks at 25.62 eV (Ta-4$f_{7/2}$) and 27.32 eV (Ta-4$f_{5/2}$) with a broad satellite peak at 28.73 eV shown in the figure 3(c). The binding energy separation (spin–orbit splitting) between two main peaks of Ta-4f orbital $\Delta E \sim 1.7$ eV suggest the pentavalent oxidation state of Ta, further it is confirmed by the electronic spectrum of Ta-4d (figure 3(d)) orbital which exhibits two peaks at 230.11 eV (Ta-4$d_{5/2}$) and 241.82 eV (Ta-4$d_{3/2}$) with a binding energy separation (spin–orbit splitting) $\Delta E \sim 11.71$ eV [25] which matches with the values reported in literature.

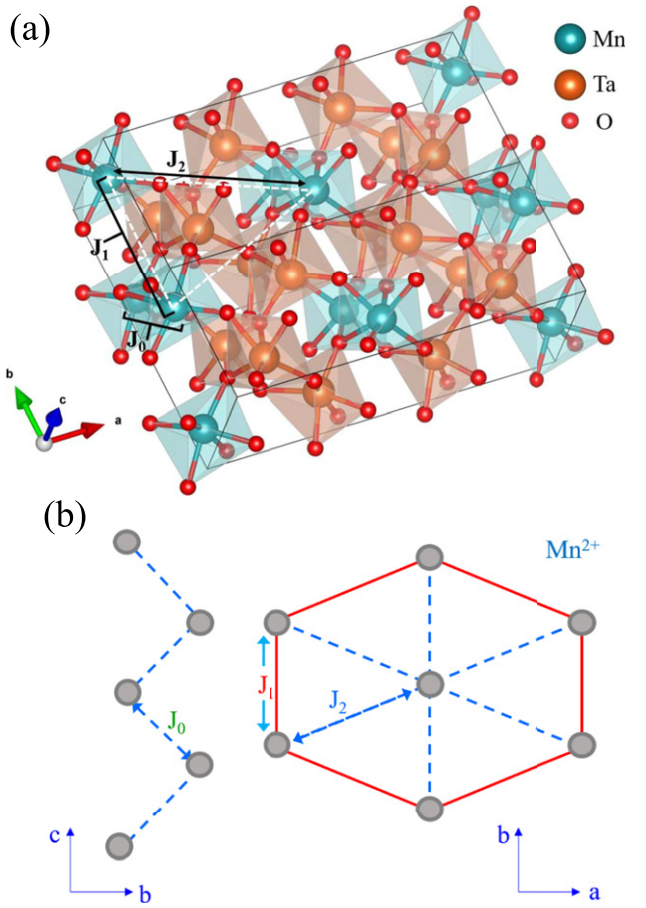

Figure 2. (a) Schematic of the two-unit cells of $MnTa_2O_6$ and the arrows in black colour represent the locus of exchange interaction paths within the given unit cell. (b) The bottom vector diagram demonstrates the intra-chain exchange interaction J_0 pointing along the c-axis in zig-zag path and the inter-chain exchange interactions J_1 and J_2 are shown in the ab-plane of orthorhombic unit cell.

3. Temperature variation of heat capacity near Neel temperature

The heat capacity $C_P(T)$ measurements of the $MnTa_2O_6$ sample were recorded from 1.9 K to 12 K by using the standard heat-pulse calorimetry [26] in physical property measurement system (PPMS) of Quantum Design. A dual-slope analysis was implemented near the transition temperature to observe the magnetic field effect on phase transition. In this technique, the heat capacity of the sample is measured directly by comparing the heating and cooling rates of the sample temperature without explicit use of the thermal conductance between sample and bath [27]. The temperature dependence of heat capacity $C_P(T)$ curves for $H = 0$ and $H = 90$ kOe are plotted in the figure 4 indicating a clear distinct peak for both the fields. The C_P curve for $H = 0$ shows transition at $T_N = 6.00 \pm 0.02$ K which is in excellent agreement with $T_N = 5.97 \pm 0.06$ K determined from $\partial(\chi T)/\partial T$ vs T plot for $H = 500$ Oe as shown later. Similarly, the transition temperature at $T_N = 5.47 \pm 0.02$ K obtained from C_P vs T plots for $H = 90$ kOe is also in line with $T_N = 5.53 \pm 0.06$

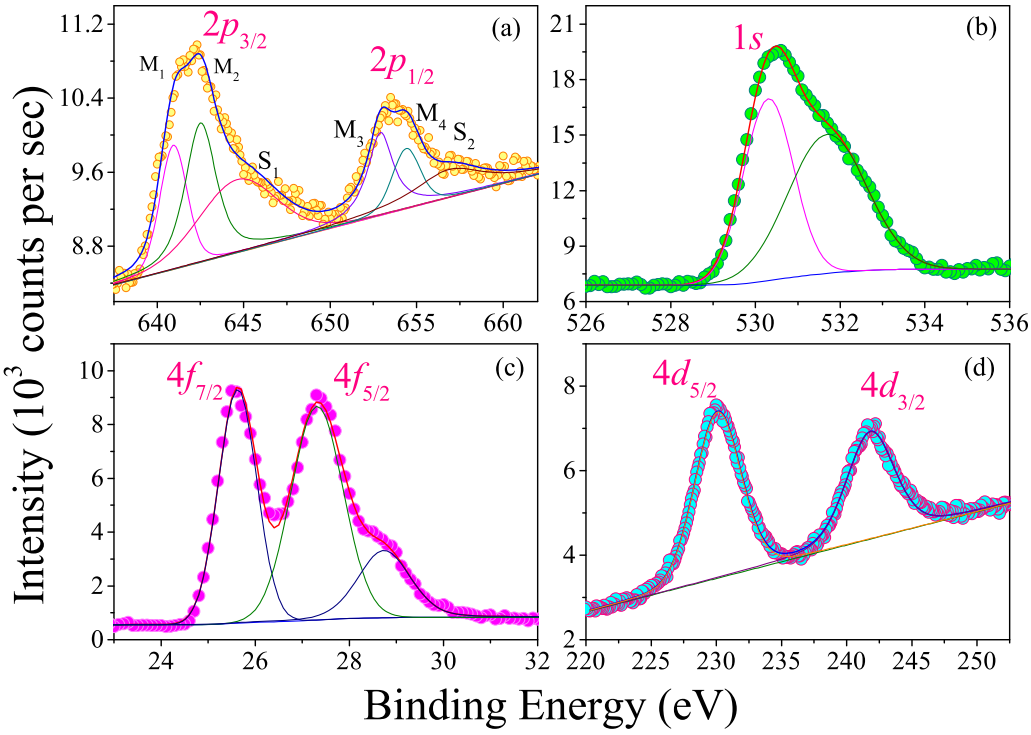

Figure 3. X-ray photoelectron spectra plotted in terms of photoelectron intensity versus binding energy (eV) of core-level (a) Mn-2p, (b) O-1 s (c) Ta-4f and (d) Ta-4d ions in the polycrystalline $MnTa_2O_6$.

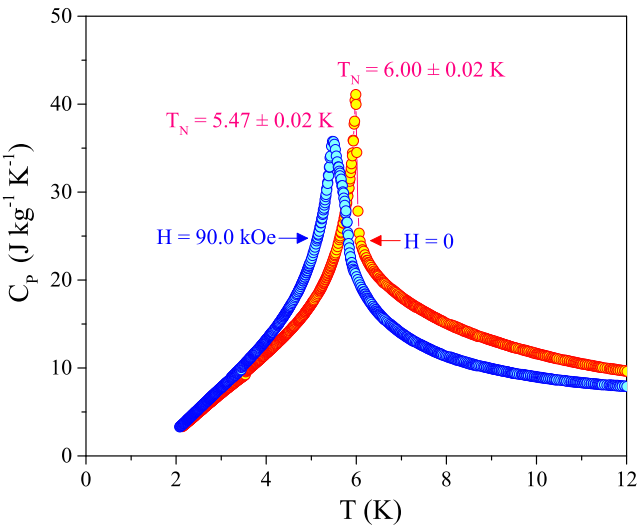

Figure 4. Thermal variation of specific heat $C_P(T)$ data measured for $H = 0$ and $H = 90$ kOe showing the antiferromagnetic to paramagnetic phase transition at $T_N = 6.00 \pm 0.02$ K and $T_N = 5.47 \pm 0.02$ K, respectively.

K obtained from $\partial(\chi T)/\partial T$ vs T plot which are shown later in the H–Tdiagram.

For a second-order phase transition, the temperature dependence of heat capacity $C_P(T)$ near transition temperature is usually fit to the equation: $C_P = A(T - T_N)^{-\alpha}$ where A is a constant and α is the critical exponent [28]. The slope of linear fit to the log–log plots of C_P vs $|T - T_N|$ gives the value of α for both $T > T_N$ and $T < T_N$ as shown in the figure 5. Since the linear fit is very sensitive to the selection of transition temperature T_N, we varied T_N from 5.96 K to 6.00 K in steps of 0.01 K to get the best linear fit for the determination of better α values. From the log–log plots of C_P vs $|T - T_N|$ for $T_N = 6.00$ K (see figure 5), linear fits are obtained yielding $\alpha = 0.13(1)$ for $T < T_N$ valid in the range of $0.025 < |T - T_N| < 0.15$ and $\alpha = 0.106(2)$ valid for somewhat larger range of $0.04 < |T - T_N| < 0.5$ for $T > T_N$. Similar magnitudes of α have been reported in antiferromagnets MnF_2 [28] with $\alpha = 0.18(0.16)$ for $T < T_N(T > T_N)$ and in $MnNb_2O_6$ [18] with $\alpha = 0.15(0.12)$ for $T < T_N(T > T_N)$.

4. Electron spin resonance spectroscopy

The electron spin resonance (ESR) measurements of the sample were carried out at room temperature using an X-band spectrometer of model: JES-FA200 (JEOL) at IIT Guwahati, India. The spectrum obtained for $MnTa_2O_6$ using frequency $f = 9.4$ GHz is shown in figure 6, along with its fit to the Lorentzian line-shape expected for exchange-narrowed linewidths in insulators. An excellent fit is obtained to the Lorentzian line-shape with peak-to-peak linewidth $\Delta H_{PP} = 936(1)$ Oe, and resonance field $H_r = 3332.3(1)$ Oe. Using the standard resonance equation $h.f = g.\mu_B.H_r$ (h = Planck's constant, μ_B = Bohr magneton) [29], $g = 2.0155(2)$ is obtained as the g-value for Mn^{2+} which is characteristic of the $^6S_{5/2}$ ground state of Mn^{2+}. This g-value is also in excellent agreement with $g = 2.015(5)$ obtained from the analysis of the temperature dependence of the magnetic susceptibility above T_N as shown later. Temperature dependence of the ESR spectra

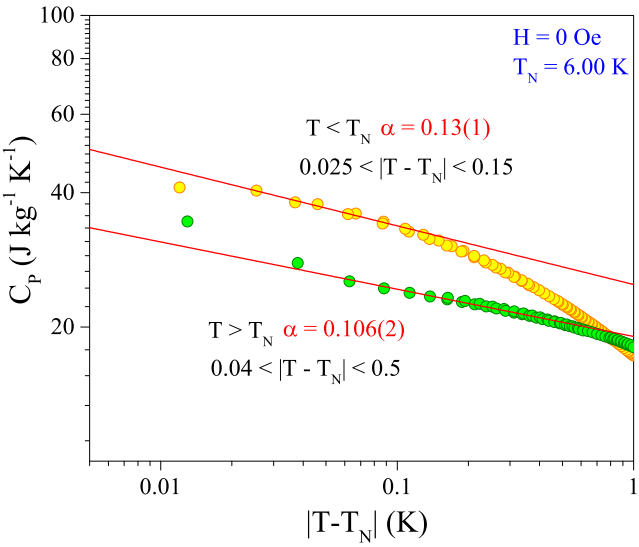

Figure 5. The temperature dependence of C_P near T_N is fit to the equation: $C_P = A|T - T_N|^{-\alpha}$ using log–log plot of C_P vs $|T - T_N|$ with the linear fits shown in the figure yielding the exponent α for both $T > T_N$ and $T < T_N$. The ranges for the validity of α are also listed in the figure.

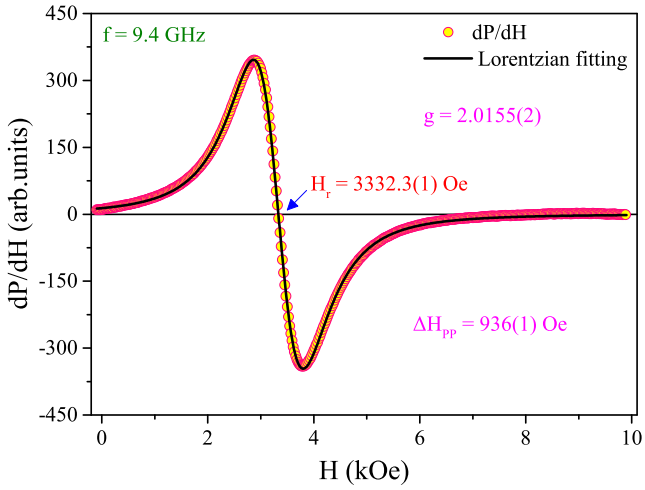

Figure 6. The room temperature electron spin resonance (ESR) spectra of $MnTa_2O_6$ plotted as first derivative of absorption intensity (P) versus magnetic field (H). The solid line is fit to Lorentzian line-shape given by: $dP/dH = [-2P_M(H - H_r)(\Delta H)^2]/[(H - H_r)^2 + (\Delta H)^2]^2$, with $\Delta H = \frac{(\sqrt{3})\Delta H_{PP}}{2}$.

could not be done because of lack of appropriate experimental facilities.

5. Temperature and magnetic field dependence of magnetization

Magnetic measurements of $MnTa_2O_6$ were carried out using a vibrating sample magnetometer (VSM) mode-based physical property measurement system (PPMS) from Quantum Design (PPMS DynaCool), which has the capacity of magnetic fields (DC) ranging from −90 kOe to 90 kOe and the temperature variation between 1.9 K to 400 K. For the magnetization (M) versus temperature (T) measurements, the sample was cooled to 1.9 K from room temperature in the presence of zero magnetic field. After cooling, a non-zero magnetic field is applied, and the magnetic moments are recorded with increasing temperature in small temperature steps of $\Delta T = 0.06$ K. The step size in magnetic field (H) used for isothermal M vs H measurements was 50 Oe up to ±90 kOe. Additional measurements of magnetization in H up to 250 kOe at 1.5 K were done at National High Magnetic Field Laboratory (NHMFL) located at the Florida State University in Tallahassee (Florida), USA.

5.1. Magnetic field dependence of the Néel temperature

The temperature variation of magnetic susceptibility $\chi = M/H$ at the magnetic field $H = 500$ Oe in the temperature range from 1.9 K to 8 K covering the temperature around T_N is shown in figure 7(a). The plot indicates a clear change in the slope near 6 K marked by arrow which indicated onset of magnetic ordering from the paramagnetic (PM) to antiferromagnetic (AFM) state. However, the position of the Néel temperature T_N is accurately determined by $\partial(\chi T)/\partial T$ vs T plots because χT represent the magnetic energy and so peaks in both $\partial(\chi T)/\partial T$ vs T and C_P vs T plots have the same physical meaning [18, 30–33]. In AFM systems, the position of the maximum in the magnetic susceptibility (peak T_P in the χ vs T plot) usually occurs above T_N [33], which in this case occurs at $T_P \sim 10.5$ K as evident in inset of figure 7(a). The plot of the computed $\partial(\chi T)/\partial T$ vs T shown in figure 7(b) yields the peak at $T_N = 5.97 \pm 0.06$ K, in close agreement with $T_N = 6.00 \pm 0.02$ K determined from the temperature dependence of the specific heat in figures 4 and 5. This value is slightly larger than $T_N = 5.7$ K reported by Scharf *et al* [19] in 1976. Similar analysis of determining T_N from the computed $\partial(\chi T)/\partial T$ vs T plots was carried out to determine the H—dependence of T_N up to $H = 90$ kOe and this T_N vs H variation is used in complete mapping of H–T phase diagram, following our recent measurements in $MnNb_2O_6$ [18] and earlier measurements reported in AFM MnF_2 [34, 35]. Further discussion on the H–T phase diagram is presented later.

For lower H values, T_N is expected to decrease linearly with increase in H according to the following equation based on the molecular field theory (MFT) [31, 34–36]:

$$T_N(H) = T_N(0) - D_1 H^2 \tag{2}$$

$$D_1 = \frac{g^2 \mu_B^2 (2S^2 + 2S + 1)}{40 k_B^2 T_N}. \tag{3}$$

For $MnTa_2O_6$, the plot of T_N determined from the peaks in $\partial(\chi T)/\partial T$ vs T data for different H vs H^2 is shown in figure 8. From the slope and intercept of linear fit to the equation (2) as shown in figure 8, $D_1 = 0.326(5) \times 10^{-9}$ K/Oe^2 and $T_N(0) = 5.97$ K are obtained. Similar analysis for some other antiferromagnets has been previously reported yielding $D_1 = 7.3 \times 10^{-9}$ K/Oe^2 for Er_2O_3 [31], $D_1 = 0.159 \times 10^{-9}$ K/Oe^2 for MnF_2 [34, 35], $D_1 = 0.66 \times 10^{-9}$ K/Oe^2 for $GeCo_2O_4$ [36] and $D_1 = 0.9 \times 10^{-9}$ K/Oe^2 for $MnNb_2O_6$ [18]. Using equation (3) with $g = 2.0155$ and $S = 5/2$ for $MnTa_2O_6$ yields

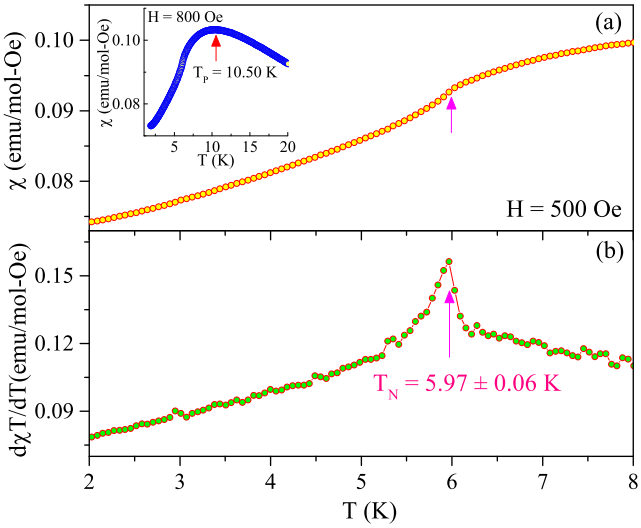

Figure 7. (a) Temperature variation of the dc-susceptibility $\chi(T)$ measured under zero-field-cooled (ZFC) condition at $H = 500$ Oe. (b) Computed plot of $\partial(\chi T)/\partial T$ versus T showing a peak corresponding to $T_N = 5.97$ K. The inset of figure (a) shows $\chi_{ZFC}(T)$ vs T measured at $H = 800$ Oe with broad peak at $T_P = 10.50$ K marked by arrow.

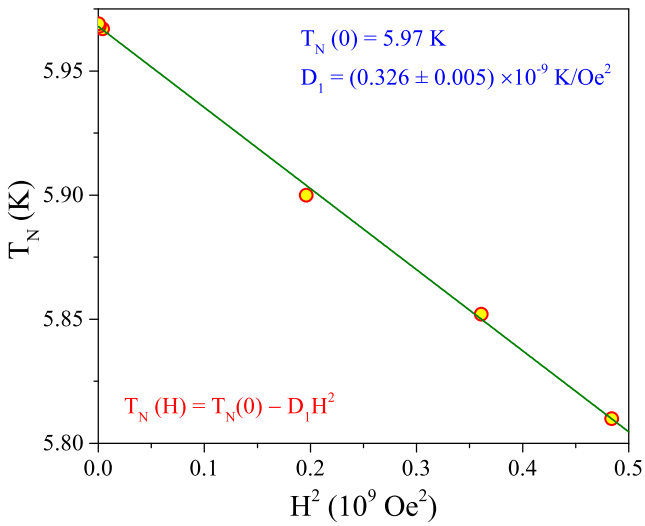

Figure 8. The plot of T_N vs H^2. The solid green line represents the linear fit of the experimental data to the equation $T_N(H) = T_N(0) - D_1H^2$ with magnitudes of evaluated parameters listed.

calculated $D_1 = 1.41 \times 10^{-9}$ K/Oe^2 which is in fair agreement with the experimental value $D_1 = 0.326(5) \times 10^{-9}$ K/Oe^2 determined above. In all the above noted cases, the calculated D_1 using equation (3) is somewhat larger than the experimental value. This difference has been assigned to the inadequacy of molecular field theory near T_N, since long-range spin correlations which develop on approach to T_N are not properly taken into account in MFT.

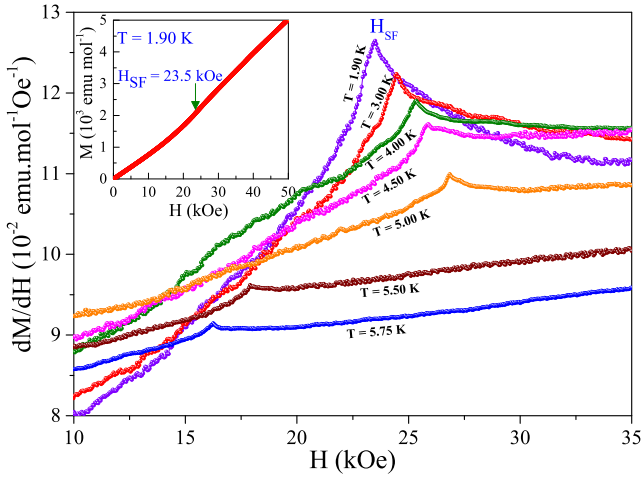

Figure 9. The plots of computed $(\partial M/\partial H)$ vs H using the data of the isothermal M vs H variations for different temperatures between 1.9 K and 5.75 K (the inset shows data at 1.9 K). The peaks correspond to the spin-flop field, H_{SF}.

5.2. Spin-flop field and its temperature dependence

The magnetic field dependence of magnetization $M(H)$ up to 50 kOe at 1.9 K is shown in the inset of figure 9, with similar measurements have been done for different temperatures below T_N. The M–H isotherm in the inset of figure 9 shows clear variation of slope near 23.5 kOe, which is evident in the peak of the computed $\partial M/\partial H$ vs H curve showing a peak at $H_{SF} = 23.5$ kOe. For $H > H_{SF}$ applied along the easy direction, the spins flop to a direction perpendicular to the applied H, although the overall ordering of the spins is still antiferromagnetic. For a polycrystalline sample, the peak in $\partial M/\partial H$ at H_{SF} is weaker than that in a single crystal since only a fraction of the grains have their easy direction oriented parallel to the applied field. The $\partial M/\partial H$ vs H curves for different $T < T_N$ are plotted in the figure 9 and the field corresponding to the peaks in these curves are indicated as spin-flop field (H_{SF}). The magnitude of H_{SF} shows a weak temperature dependence as temperature approached T_N, a trend like that observed in antiferromagnets like MnF_2 [34, 35] and $MnNb_2O_6$ [18]. The plot of this temperature dependence is given in the next section.

5.3. H–T phase diagram

The computed plots of the $\partial(\chi T)/\partial T$ vs T for $H > 17$ kOe are shown in figure 10, the peaks in these plots signifying the variation of T_N with $H > 17$ kOe. Using the H_{SF} vs T and T_N vs H variations obtained from the peaks in $\partial M/\partial H$ vs H and $\partial(\chi T)/\partial T$ vs T plots respectively, the obtained H–T phase diagram of $MnTa_2O_6$ is shown in the figure 11. This plot shows the triple point $T_{TP}(H, T) = (17.0$ kOe, 5.69 K) for $MnTa_2O_6$ where the three phases namely AFM, spin-flop and PM coexist. In this plot we have included the data point of $T_N = 5.47$ K measured at $H = 90$ kOe using the

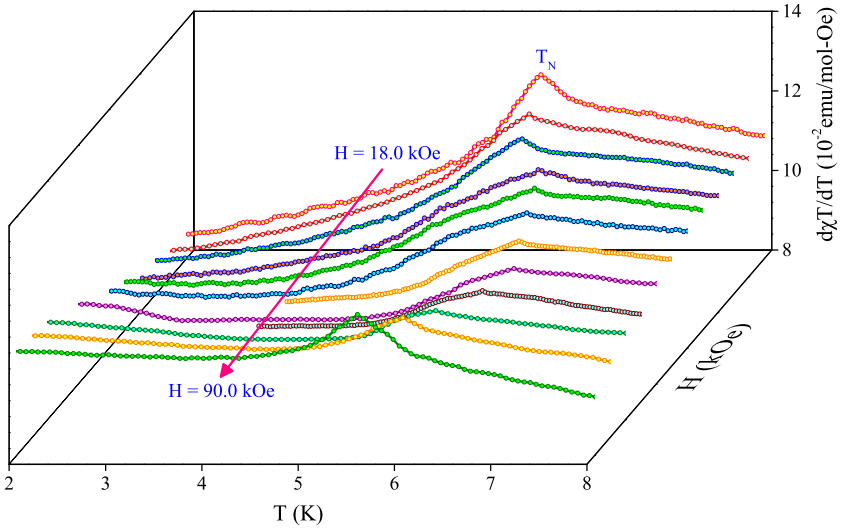

Figure 10. Temperature dependence of the computed curves of $\partial(\chi T)/\partial T$ vs temperature using the measured M vs T plots at $H > H_{TP}$ (17.0 kOe). The plots shown are for H (kOe) = 18, 20, 22, 24, 26, 28, 35, 40, 50, 60, 70 and 90, with the peak representing T_N.

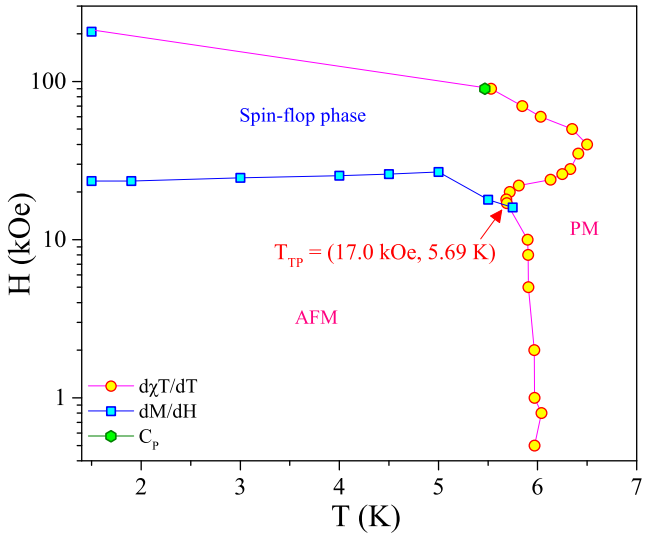

Figure 11. H–T phase diagram of polycrystalline $MnTa_2O_6$ sample yielding triple point, $T_{TP}(H, T) = (17.0$ kOe, 5.69 K) with the source of the data points marked in the legend. Lines connecting the data points are visual guides and PM = paramagnetic and AFM = antiferromagnetic.

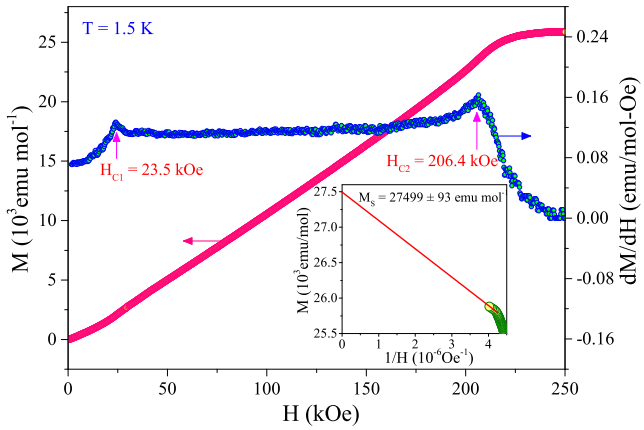

Figure 12. Isothermal ($T = 1.5$ K) M vs H plot recorded at the NHMFL and the computed plot of dM/dH versus H yielding the two critical fields at $H_{C1} = 23.5$ kOe and $H_{C2} = 206.4$ kOe. Inset shows the plot of M vs $1/H$ at $T = 1.5$ K for $H > 220$ kOe to estimate the saturation magnetization M_S in the limit of $1/H \to 0$.

specific heat measurements (see figure 4) and M vs H data up to $H = 250$ kOe and $T = 1.5$ K measured at the NHMFL (figure 12). Qualitatively, the H–T phase diagram of figure 11 for $MnTa_2O_6$ is like that reported recently in $MnNb_2O_6$ with the $T_{TP}(H,T) = (18.0$ kOe, 4.06 K) and $T_N(0) = 4.36$ K except that in $MnTa_2O_6$, the increase in T_N for $H > T_{TP}(H,T)$ is more pronounced than that observed in $MnNb_2O_6$ [18] and even in MnF_2 [34, 35]. This point is evident in the comparative comparison of the H–T phase diagrams of $MnTa_2O_6$ and $MnNb_2O_6$ when plotted in the reduced temperature scale of $T/T_N(0)$ as done in figure 13. The determination of this H–T phase diagram for $MnTa_2O_6$ is an important result of this work.

5.4. Temperature variation of the paramagnetic susceptibility

For applied $H = 800$ Oe, the temperature variation of magnetic susceptibility $\chi = M/H$ of $MnTa_2O_6$ between 1.9 K and 400 K is shown in figure 14. The analysis of χ vs T for $T > T_N$ was done based on the modified Curie–Weiss (CW) law [18]:

$$\chi = \chi_0 + \frac{C}{T - \theta}. \tag{4}$$

Here θ and C are the Curie–Weiss temperature and Curie constant respectively and $\chi_0 = \chi_{vv} + \chi_d$ [36, 37] has contributions from both Van-Vleck susceptibility (χ_{vv}) and diamagnetic susceptibility (χ_d). Van-Vleck susceptibility (positive sign) arises when the systems have non-zero orbital angular momentum ($L \neq 0$) i.e. due to spin–orbit coupling whereas all systems have a (negative) diamagnetic susceptibility. In $MnTa_2O_6$ only Mn^{2+} contributes to the magnetic properties

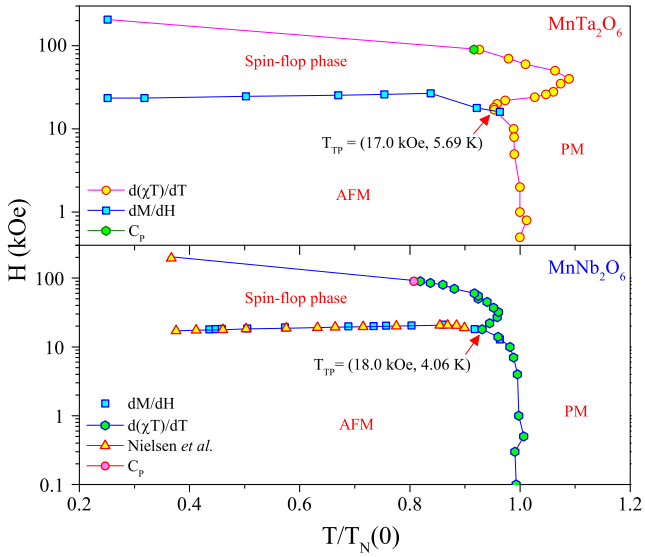

Figure 13. The H–T phase diagrams of $MnTa_2O_6$ determined in this work (top) is compared with that of isostructural $MnNb_2O_6$ (bottom) reported recently in reference [18] by Maruthi *et al*. The reduced temperature scale of $T/T_N(0)$ with $T_N(0) = 6.00$ K and 4.36 K for $H = 0$ Oe for $MnTa_2O_6$ and $MnNb_2O_6$ respectively is used and parameters of the triple point are listed in the figures. See text for discussion.

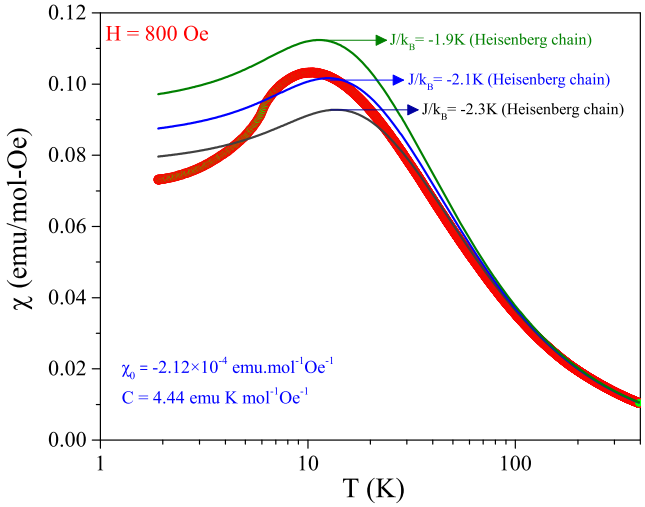

Figure 14. Temperature dependence of magnetic susceptibility $\chi(T)$ recorded under ZFC mode at $H = 800$ Oe covering the maximum temperature range from 1.9 K to 400 K (red circles). The three solid lines are the fits to Heisenberg linear chain model given by equation (9) for different J/k_B values.

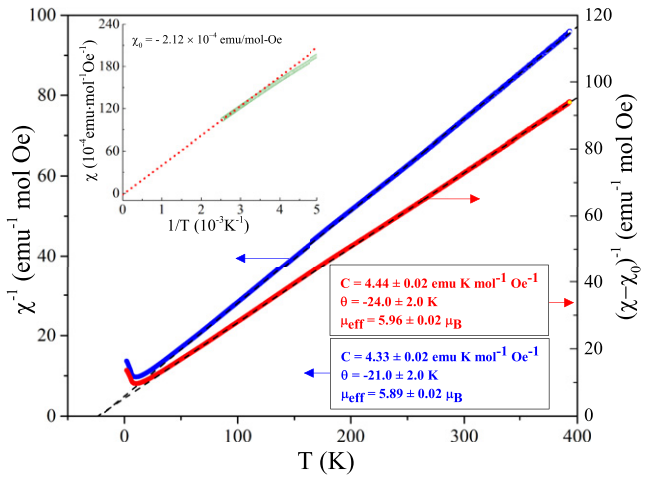

Figure 15. Plots of the temperature variation of inverse magnetic susceptibility $(\chi - \chi_0)^{-1}$ for $\chi_0 = 0$ and $-0.000\,212$ emu mol^{-1} Oe^{-1}. Dotted lines represent the linear fits to modified CW law, equation (4), for T above ~25 K yielding the magnitude of C and θ listed in the figure. Note that different y-scales for the two cases are used to separate the two plots. The inset shows linear extrapolation of χ in the limit $1/T \to 0$ using the high-T points to determine χ_0.

whereas Ta^{5+} is non-magnetic. The electronic configuration of Mn^{2+} is given as [Ar]$3d^5$ and the corresponding ground state spectral term is $^6S_{5/2}(L = 0)$ [38]. Therefore, spin–orbit coupling does not contribute to the magnetic moment to first order as also confirmed by the $g = 2.0155$ observed in the ESR experiments (figure 6). Hence it is expected that in $MnTa_2O_6$,$\chi_{vv} = 0$. The value of $\chi_0 = \chi_d = -2.1262 \times 10^{-4}$ emu mol^{-1} Oe^{-1} is estimated theoretically by adding the diamagnetic contribution of each atom [39]. Experimental determination of χ_0 is done by linear extrapolation of χ to χ_0 in the limit of $1/T = 0$ in the χ vs $1/T$ plot focussing on high temperature regime as shown in the inset of figure 15. This yields experimental $\chi_0 = -2.12 \times 10^{-4}$ emu mol^{-1} Oe^{-1} value, in agreement with the theoretical value. The CW linear fit for the plots of $(\chi - \chi_0)^{-1}$ vs T in the paramagnetic region for both $\chi_0 = -2.12 \times 10^{-4}$ emu mol^{-1} Oe^{-1} and $\chi_0 = 0$ are shown in the figure 15, with the intercept yielding θ and the slope yielding C. For $T > 25$ K, the linear fit for $\chi_0 = -2.12 \times 10^{-4}$ emu mol^{-1} Oe^{-1} yields $\theta = -24.0 \pm 2.0$ K, and $C = 4.44 \pm 0.02$ emu K mol^{-1} Oe^{-1} and for $\chi_0 = 0$,$\theta = -21.0 \pm 2.0$ K and $C = 4.33 \pm 0.02$ emu K mol^{-1} Oe^{-1} are obtained. The effective magnetic moment μ_{eff} is determined from the equation $C = N_A\mu_{eff}^2/3k_B$ (k_B = Boltzmann constant, N_A = Avogadro's number) [18] yielding $\mu_{eff} = 5.89 \pm 0.02\ \mu_B$ per formula unit (f.u.) for $\chi_0 = 0$ and $\mu_{eff} = 5.96 \pm 0.02\ \mu_B$/(f.u.) for $\chi_0 = -2.12 \times 10^{-4}$ emu mol^{-1} Oe^{-1}. The latter is in excellent agreement with $\mu_{eff} = 5.962\ \mu_B$ calculated from the equation $\mu^2 = g^2\mu_B^2 S(S+1)$ using $S = 5/2$ for Mn^{2+} and the $g = 2.0155$ obtained here from ESR measurements, providing additional confidence in this analysis. Hence including the effect of χ_0 leads to the more accurate determination of θ,C and μ_{eff} values.

5.5. Saturation magnetization and anisotropy field

From the M vs H variation of figure 12 for H up to 250 kOe at temperature 1.5 K, the computed $\partial M/\partial H$ vs H plot yields two critical fields: the spin-flop field H_{SF} or $H_{C1} = 23.5$ kOe and $H_{C2} = 206.4$ kOe. As already described in section 5.2, H_{SF} is not a spin-flip transition which occurs from an antiferromagnetic (AFM) to ferromagnetic state resulting in considerably larger change in magnetization [40] than what is observed in $MnTa_2O_6$,H_{SF} is a spin-flop transition to another AFM state, and only for $H > H_{C2}$, all the spins are forced to orient in the magnetic field direction

thus overcoming the exchange coupling field H_E leading to forced ferromagnetism and saturation magnetization. The linear extrapolation of magnetization (M) in the M vs $1/H$ plot yields saturation magnetization $M_S = 27\,499 \pm 93$ emu mol^{-1} in the limit of $1/H = 0$ and so $H_E = H_{C2} = 206.4$ kOe. The equation $M_S = \chi_\perp H_E$ [40] yields perpendicular susceptibility $\chi_\perp = 0.133$ emu/mol Oe which is approximately equal to the peak value of χ at 10.5 K just above the transition temperature shown in the inset of figure 7(a). This is corroborated by the reported data in single crystal of antiferromagnetic MnF_2 in which the susceptibility ($\chi_\perp$) perpendicular to easy axis is found to be nearly temperature independent below T_N and so it is nearly equal to the peak value of χ just above T_N. Using $H_E = H_{C2} = 206.4$ kOe and $H_{SF} = 23.5$ kOe, the anisotropy field $H_A = 1.34$ kOe is estimated for $MnTa_2O_6$ from the relation $H_{SF} = (2H_AH_E)^{1/2}$ [18, 31, 35]. At $T = 0$ K, the calculated saturation magnetization $M_S = N_A.g.\mu_B.S$ for complete alignment of the spins for $H > H_E$, using $g = 2.0155$ and $S = 5/2$,$M_S = 28\,141$ emu mol^{-1} is obtained which is only 2.3(3)% larger the measured $M_S = 27\,499 \pm 93$ emu mol^{-1} at 1.5 K. This small difference is likely due to the temperature dependence of M_S which is expected to decrease with increase in temperature. This good agreement between the measured and calculated M_S leads us to conclude that in $MnTa_2O_6$, the ground state of Mn^{2+} has effective spin $S = 5/2$ with $g = 2.0155$, like in $MnNb_2O_6$ [18].

5.6. Determination of exchange constants

In $MnTa_2O_6$, as in $MnNb_2O_6$,Mn^{2+} ion has high spin $S = 5/2$ state. Therefore, molecular field theory (MFT) which becomes more appropriate for classical (large) spins can be applied for the estimation of exchange constants in this compound. Using the exchange Hamiltonian given in equation (1), the following expressions for θ and T_N using molecular field theory are obtained [18, 40, 41]:

$$3k_B\theta = S(S+1)[J_0Z_0 + (J_1Z_1 + J_2Z_2)] \quad (5)$$

$$3k_BT_N = S(S+1)[J_0Z_0 - (J_1Z_1 + J_2Z_2)]. \quad (6)$$

Here J_0 is the nearest neighbour exchange interaction among Mn^{2+} ions along the c-axis with nearest neighbours $Z_0 = 2$ where as J_1 and J_2 are the interchain exchange interactions among Mn^{2+} ions along the b-axis with nearest neighbours $Z_1 = 2$ and along the body-diagonal in the ab-plane with next-nearest neighbours $Z_2 = 4$ respectively. Equations (5) and (6) have three exchange constants J_0,J_1 and J_2 and known values of θ and T_N are available from the Curie Weiss fit. Hence at best only two exchange constants can be determined. Therefore, to reduce the number of variables from 3 to 2, we make the approximation $J_1 = J_2 = J_\perp$ since as shown in figure 2, J_1 and J_2 are in the ab plane perpendicular to c-axis and have somewhat similar environment. This approximation was also made in isostructural $CoNb_2O_6$ [23] and $MnNb_2O_6$ [18]. Using $S = 5/2$,$J_1 = J_2 = J_\perp$,$Z_0 = Z_1 = 2$, and $Z_2 = 4$, equations (5) and (6) yield the following relations for J_0/k_B and $J_\perp/k_B$:

$$J_0/k_B = 3(\theta + T_N)/35 \quad (7)$$

$$J_\perp/k_B = (\theta - T_N)/35. \quad (8)$$

Substituting the experimentally determined $\theta = -24.0 \pm 2.0$ K and $T_N = 6.00$ K for $MnTa_2O_6$ in equations (7) and (8) yields $J_0/k_B = -1.5 \pm 0.2$ K and $J_\perp/k_B = -0.85 \pm 0.05$ K. For $MnNb_2O_6$ with lower $T_N = 4.36$ K yielded $J_0/k_B = -1.08$ K and $J_\perp/k_B = -0.61$ K [18]. This comparison shows that the ratio of $J_0/J_\perp$ is nearly identical in the two cases although the magnitudes of J_0/k_B and $J_\perp/k_B$ are comparatively smaller in $MnNb_2O_6$ because of its comparatively smaller magnitudes of $\theta = -17$ K and $T_N = 4.36$ K [18].

Following our analysis of χ vs T data of $MnNb_2O_6$ in terms of the Heisenberg linear chain (HLC), a similar analysis is attempted for the data in $MnTa_2O_6$ using the theoretical expression [18, 42]:

$$\chi = \chi_0 + \frac{C}{T}\left(\frac{1+\Gamma}{1-\Gamma}\right). \quad (9)$$

Here $\Gamma = \coth(y) - (1/y)$ with $y = 2JS^2/k_BT$. In this model, only a single exchange constant along the chain axis (c-axis) is considered. We fitted the experimental paramagnetic susceptibility χ vs T of $MnTa_2O_6$ with equation (9) valid for HLC and using $S = 5/2$,$\chi_0 = -2.12 \times 10^{-4}$ emu mol^{-1} Oe^{-1} and $C = 4.44$ emu K mol^{-1} Oe^{-1} obtained from the linear fits of modified CW law. The figure 14 shows the fit of susceptibility data to HLC model for different values of $J/k_B = -1.9$ K, -2.1 K and -2.3 K. The fit of the data for $J/k_B = -2.3$ K looks better compared to other J/k_B values and the fitting is very good for $T > 20$ K but for $T < 20$ K the theoretical curve with peak value near 14 K does not match with the experimental curve having peak at about 10 K for $J/k_B = -2.3$ K. From figure 14, it is evident that the HLC model gives at best a semiquantitative fit for $J/k_B = -2.3$ K. For comparison, $J_0/k_B = -1.5 \pm 0.2$ K and $J_\perp/k_B = -0.85 \pm 0.05$ K were determined earlier using molecular field theory. Since there are no other reported estimates of exchange constants in literature for $MnTa_2O_6$, the above magnitudes are the best estimates available to date in this system. Additional theoretical studies are therefore warranted for determining the exchange constants and to explain the reasons for higher T_N of $MnTa_2O_6$ vis-a-vis $MnNb_2O_6$.

6. Concluding remarks

The important results on the magnetic properties of $MnTa_2O_6$ presented here are as follows: (i) transition from the paramagnetic (PM) to antiferromagnetic (AFM) state occurs at $T_N = 6.00$ K; (ii) a complete H–T phase diagram is presented defined by the tricritical/triple point T_{TP} (H,T) = (17.0 kOe, 5.69 K), with a spin flop field $H_{SF} \simeq 23.5$ kOe and exchange field $H_E \simeq 206.4$ kOe at 1.5 K and calculated anisotropy field $H_A \simeq 1.34$ kOe; (iii) for $T > 25$ K, the χ vs T data fit well with the modified CW law yielding $\theta = -24.0 \pm 2.0$ K, and $C = 4.44 \pm 0.02$ emu K mol^{-1} Oe^{-1}, the latter yielding $\mu_{eff} = 5.96 \pm 0.02$ μ_B and $g = 2.015$ per Mn^{2+}, consistent with the ESR measurements and the $S = 5/2$ ground state of

the Mn^{2+} ions with negligible contribution for the spin–orbit coupling; (iv) molecular field theory and magnitudes of θ and T_N are used to determine the exchange constants $J_0/k_B = -1.5 \pm 0.2$ K along the c-axis and $J_\perp/k_B = -0.85 \pm 0.05$ K perpendicular to the c-axis; and (v) analysis of the specific heat data near T_N yields the critical exponent $\alpha = 0.106\,(0.13)$ for $T > T_N(T < T_N)$.

At appropriate places in this paper, comparison of these results in $MnTa_2O_6$ is made with those reported recently in isostructural compound $MnNb_2O_6$ with $T_N = 4.36$ K including the H–T phase diagram. This comparison shows two important differences. First, although the lattice constants of $MnTa_2O_6$ are somewhat larger those of $MnNb_2O_6$ as noted in the introduction, why the T_N and hence the exchange constants in $MnTa_2O_6$ are larger vis-à-vis those in $MnNb_2O_6$ is not understood. Second, there is a noticeable difference in the phase diagram of the two systems above T_{TP} (H,T) as noted in our results. Further investigations on understanding these differences are warranted.

Acknowledgments

MR acknowledge the financial support from University Grants Commission (UGC), Ministry of Education (MOE), Government of India. MR, SG and ST acknowledges the FIST programme of Department of Science and Technology, India for partial support of this work (Refs. No. SR/FST/PSII-020/2009 and No. SR/FST/PSII-037/2016). MR and SG acknowledge the Central Instrument Facility (CIF) of the Indian Institute of Technology Guwahati for partial support of this work. RM and RSR would like to acknowledge the Ministry of Education (MOE), Singapore through Grant No. MOE2019-T2-1-058 and National Research Foundation (NRF) through Grant No. NRF-CRP21-2018-0003. A portion of this work was performed at the National High Magnetic Field Laboratory, which is supported by the National Science Foundation Cooperative Agreement No. DMR-1644779 and the State of Florida. ST acknowledges Dr Sobhit Singh of Rutgers University for helpful discussions. MR and SG thank Mr Suchit Kumar Jena for his help during the PPMS measurements at IIT Guwahati.

Data availability statement

All data that support the findings of this study are included within the article.

ORCID iDs

Maruthi R https://orcid.org/0000-0002-6732-1509
Mohindar S Seehra https://orcid.org/0000-0002-6907-9584
Sayandeep Ghosh https://orcid.org/0000-0002-4695-8172
Rohit Medwal https://orcid.org/0000-0003-0648-2592
Rajdeep S Rawat https://orcid.org/0000-0002-3161-2486
Bruno Weise https://orcid.org/0000-0002-4789-2363
Eun Sang Choi https://orcid.org/0000-0001-9272-4134
Subhash Thota https://orcid.org/0000-0003-0740-2195

References

[1] Heid C, Weitzel H, Bourdarot F, Calemczuk R, Vogt T and Fuess H 1996 *J. Phys.: Condens. Matter.* **8** 10609
[2] Karmakar S, Garg A B, Sahu M, Tripathi A, Mukherjee G D, Thapa R and Behera D 2020 *J. Appl. Phys.* **128** 215902
[3] Munsie T J S *et al* 2017 *Phys. Rev.* B **96** 144417
[4] Prabhakaran D, Wondre F R and Boothroyd A T 2003 *J. Cryst. Growth* **250** 72
[5] Yaeger I, Morrish A H, Boumford C, Wong C P, Wanklyn B M and Garrard B J 1978 *Solid State Commun.* **28** 651
[6] Gulyaeva R I, Petrova S A, Chumarev V M and Selivanov E N 2020 *J. Alloys Compd.* **834** 155153
[7] White M A and Neshvad G 1991 *J. Chem. Thermodyn.* **23** 455
[8] Lee H J, Kim I T and Hong K S 1997 *J. Appl. Phys.* **36** 1318
[9] de Oliveira Neto S R, Kinast E J, Gusmao M A, dos Santos C A, Isnard O and da Cunha J B M 2007 *J. Phys.: Condens. Matter.* **19** 356210
[10] Mansurova A N, Gulyaeva R I, Chumarev V M and Petrova S A 2017 *J. Alloys Compd.* **695** 2483
[11] Tealdi C, Mozzati M C, Malavasi L, Ciabattoni T, Amantea R and Azzoni C B 2004 *Phys. Chem. Chem. Phys.* **6** 4056
[12] Liu Y, Huang S, Li X, Song H, Xu J, Zhang D and Wu X 2020 *Inorg. Chem.* **59** 18122
[13] Liu F, Yang X, Wang B, Guan Y, Liang X, Sun P and Lu G 2016 *Sensors Actuators* B **229** 200
[14] Weitzel H and Klein S 1973 *Solid State Commun.* **12** 113
[15] Nielsen O V, Johansson T, Holmes L M, Cock G J, Roeland L W and Ballman A A 1976 *J. Magn. Magn. Mater.* **1** 320
[16] Nielsen O V, Lebech B, Larsen F K, Holmes L M and Ballman A A 1976 *J. Phys. C: Solid State Phys.* **9** 2401
[17] Holmes L M, Ballman A A and Hecker R R 1972 *Solid State Commun.* **11** 409
[18] Maruthi R, Ghosh S, Seehra M S, Joshi D C, Chowdhury M R, Medwal R, Rawat R S, Weise B and Thota S 2021 *J. Phys.: Condens. Matter.* **33** 345801
[19] Scharf W and Weitzel H 1976 *Solid State Commun.* **18** 249
[20] Pullar R C 2009 *J. Am. Ceram. Soc.* **92** 563
[21] Sarvezuk P W C, Gusmão M A, da Cunha J B M and Isnard O 2012 *Phys. Rev.* B **86** 054435
[22] Kobayashi S, Okano H, Jogetsu T, Miyamoto J and Mitsuda S 2004 *Phys. Rev.* B **69** 144430
[23] Thota S, Ghosh S, Maruthi R, Joshi D C, Medwal R, Rawat R S and Seehra M S 2021 *Phys. Rev.* B **103** 064415
[24] Nesbitt H W and Banerjee D 1998 *Am. Mineral.* **83** 305
[25] Reddy G R, Balasubramanian S and Chennakesavulu K 2015 *RSC Adv.* **5** 81013
[26] Hwang J S, Lin K J and Tien C 1997 *Rev. Sci. Instrum.* **68** 94
[27] Riegel S and Weber G 1986 *J. Phys. E: Sci. Instrum.* **19** 790
[28] Kadanoff L P *et al* 1967 *Rev. Mod. Phys.* **39** 395
[29] Pilbrow J R 1984 *J. Magn. Reson.* **58** 186
[30] Bragg E E and Seehra M S 1973 *Phys. Rev.* B **7** 4197
[31] Narang V, Korakakis D and Seehra M S 2014 *J. Magn. Magn. Mater.* **368** 353
[32] Jena S K, Joshi D C, Yan Z, Qi Y, Ghosh S and Thota S 2020 *J. Appl. Phys.* **128** 073908
[33] Fisher M E 1962 *Phil. Mag.* **7** 1731
[34] Shapira Y, Foner S and Misetich A 1969 *Phys. Rev. Lett.* **23** 98
[35] Shapira Y and Foner S 1970 *Phys. Rev.* B **1** 3083

[36] Pramanik P, Ghosh S, Yanda P, Joshi D C, Pittala S, Sundaresan A, Mishra P K, Thota S and Seehra M S 2019 *Phys. Rev.* B **99** 134422
[37] Ghosh S, Joshi D C, Pramanik P, Jena S K, Pittala S, Sarkar T, Seehra M S and Thota S 2020 *J. Phys.: Condens. Matter.* **32** 485806
[38] Kataoka T *et al* 2012 *Solid State Commun.* **152** 806
[39] Mendelsohn L B, Biggs F and Mann J B 1970 *Phys. Rev.* A **2** 1130
[40] Rall J D, Seehra M S and Choi E S 2010 *Phys. Rev.* B **82** 184403
[41] Morrish A H (ed) 2001 *The Physical Principles of Magnetism* (Piscataway, NJ: IEEE) p 447
[42] Coulon C, Miyasaka H and Clérac R 2006 *Struct. Bond.* **122** 163